Journal of Materials Chemistry

Cite this: *J. Mater. Chem.*, 2012, **22**, 2081

www.rsc.org/materials

PAPER

Controlled synthesis of thorny anatase TiO_2 tubes for construction of Ag–AgBr/TiO_2 composites as highly efficient simulated solar-light photocatalyst†

Guohui Tian,[a] Yajie Chen,[a] Hong-Liang Bao,[b] Xiangying Meng,[a] Kai Pan,[a] Wei Zhou,[a] Chungui Tian,[a] Jian-Qiang Wang*[b] and Honggang Fu*[a]

Received 8th August 2011, Accepted 26th October 2011
DOI: 10.1039/c1jm13820k

This work reports on a two-stage strategy towards the controlled Ag–AgBr deposition onto thorny anatase TiO_2 tubes for excellent simulated solar-light photocatalytic activities. First, anatase TiO_2 tubes with a thorny porous external surface were prepared using rod-like $TiOSO_4 \cdot 2H_2O$ as sacrificial template and a Ti source *via* a solvothermal process followed by annealing. The formation mechanism of the anatase TiO_2 tubular precursor was investigated in detail. Then, the prepared anatase TiO_2 tubes were used as a support for loading AgBr nanoparticles using the deposition–precipitation method, and the deposited AgBr was partially reduced to Ag *via* the calcination process to fabricate the Ag–AgBr/TiO_2 tubular composites. X-Ray absorption near edge spectra (XANES), extend X-ray absorption fine structure (EXAFS) spectra and X-ray photoelectron spectroscopy (XPS) analyses indicated that both AgBr and Ag^0 components coexist in the systems. Compared with conventional nanoparticles and nanotubes, there exist abundant microcavities in the roughly parallel nanothorns of the tubes, which can contribute to the stable deposition of the Ag–AgBr nanoparticles and the formation of effective nanojunctions. These composites exhibited superior photocatalytic activity in the degradation of phenol under simulated solar-light irradiation.

1. Introduction

As an n-type wide-band gap semiconductor, TiO_2 has been widely investigated and commonly applied as a photocatalyst in environmental pollution control as it's nontoxic, highly chemically resistant, and inexpensive.[1–3] Because the photocatalytic activity of a catalyst is critically dependent on its structure and morphology,[4,5] morphology control of TiO_2 is considered to be an effective strategy of improving its photocatalytic performance. Compared with nanoparticles, tubular materials have been extensively pursued because their unique heterogeneous or hollow structures might play an important role as photocatalysts,[6–8] and lots of work has been done to prepare the nanotubes.[9–13] Among these materials, thorny porous TiO_2 tubes have attracted considerable interest because of their distinctive properties in comparison with the conventional TiO_2 nanotubes. Yu *et al.* prepared hierarchically titanate tubes by hydrothermal synthesis in the presence of H_2O_2 and NaOH using prepared titanium glycolate rods as precursor.[14] Li *et al.* also prepared the spiny mesoporous titania tubes by solvothermal alcoholysis of $TiOSO_4 \cdot xH_2SO_4 \cdot xH_2O$ in the presence of absolute ethanol, ethyl ether, and ethylene glycol.[15] Expectedly, the prepared TiO_2 tubes showed enhanced photocatalytic activity and photovoltaic performance.

However, because TiO_2 is a wide band gap semiconductor, it can only be used in the ultraviolet region.[16,17] In order to effectively utilize solar energy in the photocatalytic process, many strategies have been used to extend the photo-response of TiO_2 to the visible region.[18–23] Recently, several Ag/AgX (Cl, Br, I) composites on semiconductor metal oxide nanoparticle supports have been reported to show high photocatalytic ability under visible light.[24–27] These kind of composites provide a new idea for the design of photocatalysts, however, composite nanoparticles often lead to serious aggregation. Meanwhile, the formation of an effective interaction between the nanoparticles is difficult to achieve during the deposition. Therefore, a better system is required to overcome the above problems.

In the present work, we reported a facile synthetic approach to prepare thorny anatase TiO_2 tubes using rod-like $TiOSO_4 \cdot 2H_2O$ as both sacrificial template and Ti source by a solvothermal process followed by annealing. The formation mechanism and the effects of reaction parameters on the morphology evolution of the precursor were discussed. In order to broaden the visible-light photo-response and improve solar light photocatalytic activity, we constructed multi-component Ag–AgBr/TiO_2

[a]*Key Laboratory of Functional Inorganic Material Chemistry, Ministry of Education of the People's Republic of China, Heilongjiang University, Harbin, 150080, P. R. China. E-mail: fuhg@vip.sina.com; Fax: +86 451 8667 3647; Tel: +86 451 8660 4330*
[b]*Shanghai Synchrotron Radiation Facility (SSRF), Shanghai Institute of Applied Physics, Chinese Academy of Sciences, Shanghai, 201204, P. R. China. E-mail: wangjianqiang@sinap.ac.cn*
† Electronic supplementary information (ESI) available. See DOI: 10.1039/c1jm13820k

tubular composites using the prepared thorny anatase TiO_2 tubes as a supporting material. Compared to the conventional nanoparticles and nanotubes with slippery surfaces, the abundant microcavities which existed between the roughly parallel nanothorns of the prepared tubes contributed to the stable deposition of Ag–AgBr nanoparticles and the formation of effective nanojunctions. Moreover, the photocatalytic activities of the prepared Ag–AgBr/TiO_2 tubular composites were superior to that of the conventional Ag–AgBr/Degussa P25 nanoparticles under simulated solar-light irradiation for the degradation of phenol.

2. Experimental

2.1. Preparation of thorny anatase TiO_2 tubes

Rod-like solid $TiOSO_4 \cdot 2H_2O$ (about 1–2 μm in diameter and 5–20 μm in length) was purchased from Dandong Zhonghe Chemical plant, and other chemicals were purchased from Shanghai Chemical Regent Co. (Shanghai, China). A typical synthesis process was as follows: 0.45 g of rod-like solid $TiOSO_4 \cdot 2H_2O$ was added into the mixed solution of 20 mL methanol, 10 g of glycerol under stirring. The as-formed suspending liquid was introduced into a teflon-lined autoclave of 50 mL capacity and maintained at 120 °C for varied periods of time (1, 6, 12 and 24 h). After cooling to room temperature, the precursors were collected by centrifugation, and washed with ethanol several times to remove redundant glycerol and other organics. After drying in air at 80 °C, the precursors were calcined at 600 °C for 3 h to obtain the TiO_2 products.

2.2. Deposition of Ag–AgBr onto the thorny anatase TiO_2 tubes

All deposited samples were synthesized by the deposition–precipitation and calcination process. Briefly, 0.5 g TiO_2 was added to 60 mL of distilled water, and the suspension was sonicated for 30 min. Then 5 mL 5% polyetherimide (PEI) was added to the suspension, and sonicated for 30 min. Then, 1.3 g of KBr was added to the suspension, and stirred magnetically for 30 min. Different amounts of $AgNO_3$ in NH_4OH (20, 30, 40 and 60 mL, 25 wt% NH_3) was quickly added to the prepared mixtures, respectively. The resulting suspensions were stirred at room temperature for 12 h. All the above processes were carried out in a dark situation. The products were filtered, washed with water, then dried at 50 °C for 12 h in vacuum, and AgBr/TiO_2 composites with different AgBr contents (5%, 10%, 15% and 20 mol%) were obtained. Finally, the AgBr/TiO_2 composites were calcined in air at 500 °C for 2 h to prepare Ag–AgBr/TiO_2 composites. The corresponding samples were denoted as 5%Ag–AgBr/TiO_2, 10%Ag–AgBr/TiO_2, 15%Ag–AgBr/TiO_2 and 20% Ag–AgBr/TiO_2. For comparison, a Ag–AgBr/Degussa P25 composite was also constructed using the same method.

2.3. Characterization

The X-ray diffraction (XRD) of powder samples was examined on a Rigaku-Dmax 2500 diffractometer using Cu Ka radiation (λ = 0.15405 nm, 40 kV, 100 mA). Transmission electron microscopy (TEM) and high-resolution TEM (HRTEM) images of the samples were recorded in a JEOL 2100 microscope with a 200 kV accelerating voltage. Scanning electron microscopy (SEM) micrographs were taken using a Hitachi S-4800 instrument. UV-visible diffuse reflectance spectra (DRS) were determined by a UV/Vis/NIR spectrometer (Perkin-Elmer Lambda950). The surface elements and their electronic states of the samples were analyzed using X-ray photoelectron spectroscopy (XPS, Kratos-AXIS UL TRA DLD, Al Kα X-ray source). The surface photovoltage spectroscopy (SPS) measurements were carried out with a home-built apparatus which was described elsewhere.[28,29]

The X-ray absorption data at the Ag K-edge were recorded at room temperature in transmission mode using ion chambers at beam line BL14W1 of the Shanghai Synchrotron Radiation Facility (SSRF), China. The station was operated with a Si(311) double crystal monochromator. During the measurements, the synchrotron was operated at an energy of 3.5 GeV and a current between 150–210 mA. Energy calibrations were carried out using Ag foil for Ag K-edge. The data processing was performed using the program ATHENA. All fits to the EXAFS data were performed using the program ARTEMIS.[30]

2.4. Measurement of photocatalytic activity

The photodegradation experiments were performed in a slurry reactor containing 100 mL of 50 mg L^{-1} phenol and 0.1 g of catalyst. A 150 W xenon lamp (Institute of Electric Light Source, Beijing) was used as the solar-simulated light source, and visible light was achieved by utilizing a UV cut filter ($\lambda \geq 420$ nm). Prior to light irradiation, the suspension was kept in the dark under stirring for 30 min to ensure that an adsorption/desorption equilibrium was established. Oxygen flow was employed in all experiments as oxidant. Adequate aliquots (2 ml) of the sample were withdrawn after periodic intervals of irradiation, which were centrifuged at 10 000 rpm for 5 min, and then filtered through a Milipore filter (pore size 0.22 μm) to remove the residual catalyst particulates for analysis. The filtrates were analyzed using HPLC (Shimadzu SPD-10A) at a wavelength of 270 nm with a UV detector.

3. Results and discussion

3.1. Synthesis and characterization of thorny anatase TiO_2 tubes

Fig. 1a shows the XRD patterns of the precursors obtained from the different solvothermal reaction times. For reference, the

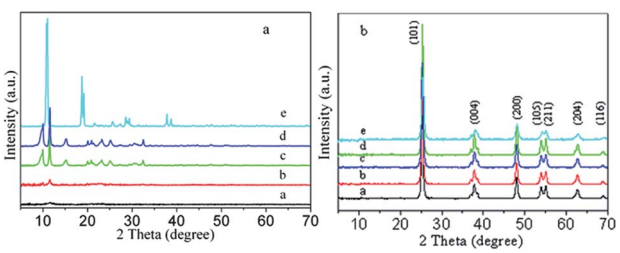

Fig. 1 XRD patterns of commercial rod-like $TiOSO_4 \cdot 2H_2O$ (e) and the precursors obtained from different solvothermal reaction times (a: 1 h; b: 6 h; c: 12 h; d: 24 h) before calcination (a) and corresponding products after calcination (b).

XRD pattern of the starting material $TiOSO_4 \cdot 2H_2O$ is also shown (curve e). There are obvious differences for the XRD patterns between $TiOSO_4 \cdot 2H_2O$ and the other precursors. The XRD pattern of $TiOSO_4 \cdot 2H_2O$ shows two strong peaks at about 10.7° and 18°. However, these peaks did not appear in the XRD patterns of the precursors, indicating the occurrence of a chemical reaction for the starting material $TiOSO_4 \cdot 2H_2O$ during the solvothermal process. When the solvothermal reaction was conducted for 1 h, no obvious peaks could be found, indicating the formation of an amorphous material (primary titanium oxyhydrate). After prolonging the solvothermal time, the XRD patterns of the precursors obtained from different solvothermal times displayed obvious sharp peaks at low 2θ angles (11.7° and 9.7°), with several weak peaks at relatively higher 2θ angles, which could not be indexed to any known structure containing titanium in the JCPDS database, but was similar to that of the reported Co, Mn, In-based glycerols.[31,32] These reports showed that the metal hydroxide could react with glycerol to form the alkoxide. Our previous study also indicated that initially formed titanium oxyhydrate in the reaction system could gradually react with glycerol to form titanium glycerolate (TiGly) coordination complexes.[33] The peak ratio changes (9.7° and 11.7°) in intensity are the indication of structure development and complete formation of the TiGly phase. After calcination at 600 °C in air for 3 h, all of the precursors transformed to anatase TiO_2 according to XRD patterns in Fig. 1b.

The morphologies of the starting material $TiOSO_4 \cdot 2H_2O$ and the precursors obtained from different reaction times were investigated by TEM and SEM. Fig. S1 shows the SEM and TEM (inset) images of the starting material $TiOSO_4 \cdot 2H_2O$,† which exhibits a rod-like morphology with a smooth surface. Fig. 2 shows the SEM images of the precursors obtained at different reaction stages, reflecting the interesting morphology evolution of the precursors obtained from different reaction times. When the reaction time is 1 h, a rod-like precursor with a relative smooth surface was obtained, which is composed of a large quantity of nanoparticles (Fig. 2a). Upon increasing the reaction time to 6 h, the surface of the rod-like precursor gradually became coarse (Fig. 2b). Moreover, as the reaction time further proceeded to 12 h, an interesting morphological variety occurred (Fig. 2c), the rod-like structure disappeared, and the rod-in-tube structure with a hollow cavity between the sheath and the core rod appeared. When increasing the reaction time to 24 h, the hollow tubular precursor with a thorny surface structure formed at the expense of the core rods (Fig. 2d). After the synthesis of the precursors, we investigated the effect of calcination on the microstructure and morphology of the precursors. As is shown from the SEM images in Fig. 3a–d, calcination did not change the integral morphology of these precursors due to the existence of plenteous O atoms in the precursors, which can directly connect to Ti^{4+}.[31,34] The corresponding TEM images shown in the inset of Fig. 3a–d further demonstrated the structure evolution process from a smooth solid rod to thorny hollow tubes. The high-magnification SEM in Fig. S2 clearly demonstrates that the external surface of the tube wall was a thorny porous structure consisting of several anatase TiO_2 nanoparticles with linear parallelism because of the removal of organic species in the precursor by pyrolysis.† Such a thorny tubular structure can act as a good catalyst support and facilitate the diffusion of reaction molecules into the interior chamber of the TiO_2 tube.

3.2. Formation mechanism of thorny titanium glycerolate tube precursor

The principal process of the morphology evolution is summarized in Fig. 4. Based on the above results, it can be concluded that a tubular structure can be obtained *via* an *in situ* reaction, dissolution–recrystallization growth process. During the solvothermal process, hydrolysis and alcoholysis reactions can happen under high pressure and high temperature conditions because of the existence of a small amount of water from the release of $TiOSO_4 \cdot 2H_2O$ and etherifying reaction between ethanol and glycerol, so amorphous titanium hydroxylated nanoparticles were formed *in situ* and aggregated to form nanorods with rough surfaces. There are numerous small protuberances on the surfaces of the nanorods, which provide many high-energy sites for nanocrystalline growth.[33,35] Then the formed titanium hydroxylated gradually reacted with glycerol to form TiGly complexes by replacing the hydroxyls in the titanium hydroxylated because the metal hydroxide can react with glycerol to form the alkoxide, which was proved by other groups and our previous study.[31–33] The formed TiGly complexes would spontaneously nucleate onto the small protuberances.

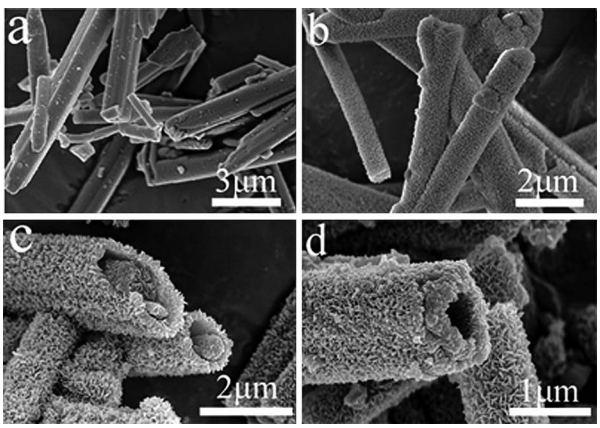

Fig. 2 SEM images of the precursors prepared from different solvothermal times, (a) 1 h, (b) 6 h, (c) 12 h and (d) 24 h.

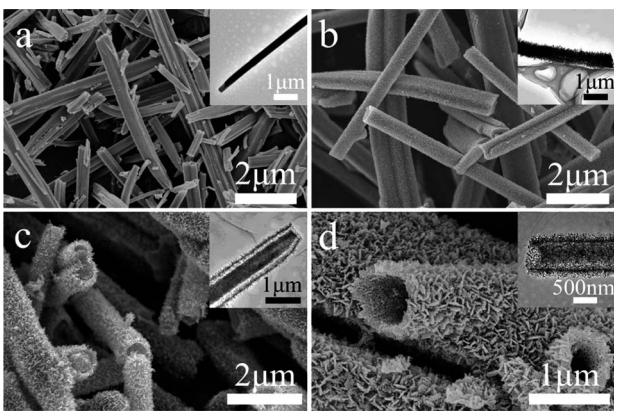

Fig. 3 SEM and TEM (inset) images of the calcined precursors prepared from different solvothermal times, (a) 1 h, (b) 6 h, (c) 12 h, (d) 24 h.

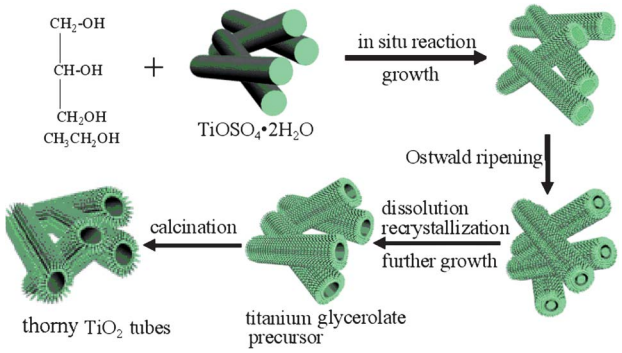

Fig. 4 Schematic illustration of the formation process of the thorny anatase TiO_2 tubes.

Furthermore, due to the anisotropic crystal structure, there was an intrinsic tendency for the nucleation growth along the 1D direction.[36] As a result, small 1D thorns formed on the surface of the rods. With the reaction going on, the inner titanium hydroxylate gradually reacted, dissolved and formed a rod-in-tube core/shell structure similar to the Ostwald ripening process. When the reaction time was further prolonged, the rod in core/shell structure gradually dissolved and the core/shell structure changed to a hollow tubular structure because of mass diffusion and Ostwald ripening. Apart from reaction time, the rod-like morphology of the starting material $TiOSO_4 \cdot 2H_2O$ was very critical in this synthesis method. To prove this assumption, the control experiment was performed using the crushed $TiOSO_4 \cdot 2H_2O$ nanoparticles as starting material. The result showed that only irregular aggregated particles were obtained (Fig. S3†), which indicates that the morphologies of the final products are closely related to the inherent crystal properties of the starting materials, and are not unambiguously determined by the synthesis method alone. In addition, glycerol is a necessary reactant. When glycerol was not used, the results showed that only rod-like precursor could be obtained, and no apparent thorny tubes were observed (Fig. S4†). It indicated that further dissolution–renucleation and growth processes did not happen because of the absence of glycerol. Therefore, the thorny TiGly tubular nanostructures could not be obtained.

3.3. Characterization of Ag–AgBr/TiO_2 tubular composites

The phase and composition of the different Ag–AgBr/TiO_2 tubular composites were characterized by XRD, as shown in Fig. S5.† All samples exhibit some diffraction peaks that are assigned to the anatase TiO_2 phase. There are two peaks with 2θ values of 30.9° and 44.4° corresponding to the (200) and (220) crystal planes of cubic AgBr (JCPDF No. 79-0149), respectively. Beside this, the very weak diffraction peak (64.4°) assigned to Ag^0 is displayed in the Ag–AgBr/TiO_2 samples.[25] The results showed the coexistence of AgBr and Ag^0 in the different Ag–AgBr/TiO_2 tubular composites.

Fig. 5 shows the Ag K-edge XANES spectra of 10%Ag–AgBr/TiO_2, Ag foil and AgBr standard. The results reveal that all the features of AgBr are present in the spectra of 10%Ag–AgBr/TiO_2 samples. Moreover, there is no apparent change among the different ratios of the Ag–AgBr/TiO_2 samples, and all XANES spectra share the same major features (see Fig. S6†). Therefore, AgBr is the main component in these samples. However, the first peak at 25520 eV in the Ag–AgBr/TiO_2 samples is broader than the AgBr standard. This kind of broad tendency mainly comes from the presence of the Ag^0 component and nano effect of AgBr. Fig. S7 shows the Fourier-transformed spectra of the k^2 weighted Ag K-edge EXAFS oscillations.† The highest peak, in the range of 2–3 Å, can be assigned to the scattering from the first nearest neighbored Br atoms and minor of Ag atoms. Further curve-fitting analyses of the data are listed in Table S1.† Compared with AgBr and 10%Ag–AgBr/TiO_2, the coordination number (CN) for Ag–Br decreases from 3.1 to 1.8 as the nano effect, while the bond distance (R) for Ag–Br remains constant at 2.78 Å, which is close to that for the AgBr reference. The CN for Ag–Ag is about 0.3 for 10%Ag–AgBr/TiO_2, which also proves the low ratio of Ag metallic particles.

Fig. S8 shows the XPS spectra of the Ag 3d regions of the different ratio of Ag–AgBr/TiO_2 samples.† Two peaks at *ca.* 367.5 and 373.5 eV in each spectrum, ascribed to Ag $3d_{5/2}$ and Ag $3d_{3/2}$ binding energies, respectively, are observed. The two peaks could be further deconvoluted into two peaks, respectively, at about 367.5, 368.5 eV and 373.5, 374.4 eV. The peaks at 367.5 and 373.5 eV are attributed to the Ag^+ of AgBr, and those at 368.5 and 374.4 eV are ascribed to the metal Ag^0. Similar results are also reported by other groups.[37,38] The spectra of Br 3d in Fig. S9 show that the binding energies of Br $3d_{3/2}$ and $3d_{5/2}$ are at ~68.8 and 67.8 eV, which are due to the crystal lattice of Br^- in AgBr.† From the XPS peak areas, the surface Ag^0, Ag^+ and Br^- content of the samples were also listed in Table S2.† The results further confirm that there are both AgBr and Ag^0 species in the systems, and the Ag species mainly exists as AgBr in all the Ag–AgBr/TiO_2 samples.

TEM was used to observe the morphology and microstructure of the Ag–AgBr/TiO_2 sample. As shown in Fig. 6b, compared with the pure thorny TiO_2 tubes (Fig. 6a), no distinct change was observed in the morphology of the Ag–AgBr/TiO_2 sample. The high magnification TEM image (Fig. 6c) shows that there are many nanoparticles on the surface of the Ag–AgBr/TiO_2 tubular composite. To further learn the component of these nanoparticles in Fig. 6c, a high-resolution TEM image from the squared area of Fig. 6c is shown in Fig. 6d. It is found that the spacings of adjacent lattice planes are consistent with the

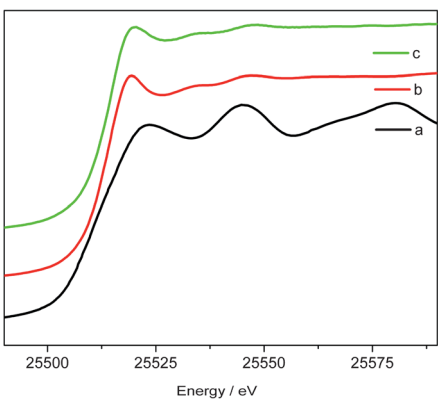

Fig. 5 Comparison of the Ag K-edge XANES spectra of the different samples: a) Ag foil, b) AgBr, c)10%Ag–AgBr/TiO_2.

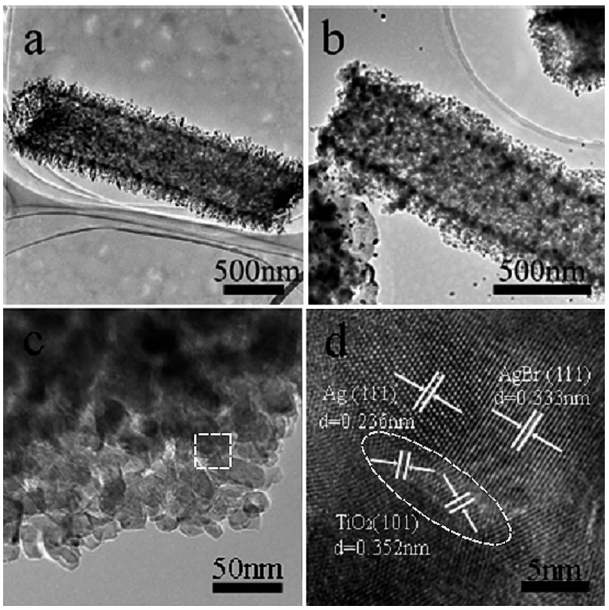

Fig. 6 TEM image (a) of the thorny anatase TiO_2 tube; TEM image (b), high magnification TEM image (c) and HRTEM image (d) of the 10% Ag–AgBr/TiO_2 sample.

interplanar distance of the (111) plane of fcc Ag (0.236 nm), the (111) plane of cubic AgBr (0.333 nm) and the (101) plane of anatase TiO_2 (0.352 nm), respectively.[39,40] It confirmed that silver nanoparticles were reduced on the surface of the silver bromide nanoparticles during calcination. Moreover, Fig. 6d shows a distinguished and coherent interface between the continuity of lattice fringes of the metallic Ag, AgBr and TiO_2 nanoparticles, indicating the formation of heterojunctions, which can benefit better charge separation and efficient electron transfer within the hybrid structure compared with binary composites and pure TiO_2.

The UV-vis absorption spectra obtained from the diffuse reflectance measurements of the TiO_2 tubes and the prepared different Ag–AgBr/TiO_2 samples are shown in Fig. 7. The UV-vis absorption spectra of the Ag–AgBr/TiO_2 samples show obvious enhanced absorption property in the visible light region compared to that of the pure thorny TiO_2 tube. The absorption peak around 290 nm assigned to the direct band gap of AgBr was overlaid by the absorption peak at about 277 nm of TiO_2.[25] The absorption band around 400–700 nm in the visible region should be assigned to surface plasmon absorption of silver and light absorption of AgBr.[25,37] One thing to be noted is that the absorbance intensity was gradually enhanced with the increase of the Ag–AgBr content in the Ag–AgBr/TiO_2 composite.

SPS can be regarded as an effective approach to understand the separation capacity of the photoinduced carriers. On the basis of the SPS principle, it can be expected that the stronger the SPS response, the higher the photoinduced charge carriers.[41,42] The SPS responses of different photocatalysts are shown in Fig. 8. It can be seen that thorny TiO_2 tube displays obvious SPS response peaks at about 345 nm, which are attributed to the electronic transitions from the valence band to conduction band (O_{2p} → Ti_{3d}) according to TiO_2 energy band structure.[43] Meanwhile, the peak has obviously red shift, and a wide marked

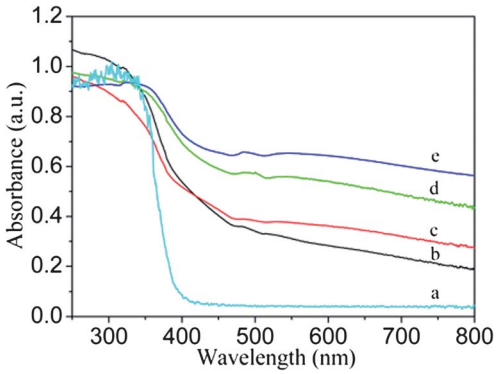

Fig. 7 UV-visible absorption spectra of different samples, a) thorny TiO_2 tubes, b) 5%Ag–AgBr/TiO_2, c) 10%Ag–AgBr/TiO_2, d) 15%Ag–AgBr/TiO_2, (e) 20%Ag–AgBr/TiO_2.

SPS response peak appears at about 420 nm in the Ag–AgBr/TiO_2 samples. This phenomenon could be analyzed by the theory of density of states.[44] It is expected that the interesting SPS peak results from the AgBr, which is further proved by the SPS of AgBr in the inset of Fig. 8. The stronger photovoltage intensity of the SPS of the Ag–AgBr/TiO_2 samples indicates higher charge separation efficiency and longer excitation lifetimes compared with pure thorny TiO_2 tubes. It is because Ag^0 deposited on the surface of thorny TiO_2 tubes can trap the photoinduced electrons and improve the charge transfer and separation. However, the SPS response gradually decreases with the further increase of Ag–AgBr content, this probably resulted from excessive trapping sites caused by the increased Ag–AgBr content in the Ag–AgBr/TiO_2 composite, which facilitated the recombination of photo-induced electrons and holes.

3.4. Photocatalytic activity test

Phenol, a widely used organic pollutant, was chosen as a representative pollutant to evaluate the photocatalytic performance of the as-prepared photocatalysts under simulated solar light illumination. To demonstrate the structure-induced enhancement of the photocatalytic performance of the Ag–AgBr/TiO_2 tubular composite, the control samples, 10%Ag–AgBr/Degussa P25 prepared using the same method and the crushed

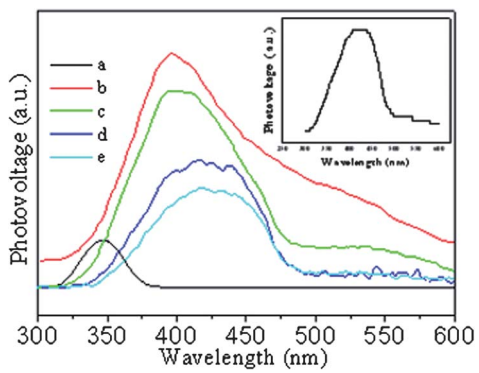

Fig. 8 SPS spectra of the different samples, a) thorny TiO_2 tube, b) 5% Ag–AgBr/TiO_2, c) 10%Ag–AgBr/TiO_2, d) 15%Ag–AgBr/TiO_2, (e) 20% Ag–AgBr/TiO_2; inset is the SPS spectrum of AgBr.

10%Ag–AgBr/TiO_2 composite nanoparticles were also used as photocatalysts. As shown in Fig. 9, C_0 and C are the initial concentration after the equilibrium absorption and the reaction concentration of phenol, respectively. The thorny Ag–AgBr/TiO_2 tubular composites exhibit higher photocatalytic activity than 10%Ag–AgBr/Degussa P25 and the crushed 10%Ag–AgBr/TiO_2 nanoparticles composites. *Via* pseudo-first-order linear fit, the determined reaction rate constant, k, which was used to evaluate the degradation rate, for the 10%Ag–AgBr/TiO_2 sample (0.07161 min^{-1}), was much higher than that for the control sample 10%Ag–AgBr/Degussa P25 (0.03157 min^{-1}) and the crushed 10%Ag–AgBr/TiO_2 (0.05426 min^{-1}), and 100% of phenol can be degraded after 45 min under simulated solar-light irradiation. The outstanding photocatalytic activities of the Ag–AgBr/TiO_2 samples can be attributed to its special structural features. Firstly, the thorny porous tubular structure can act as good buffering reservoirs for the stable incorporation of AgBr and Ag nanoparticles and contribute to the formation of effective nanojunctions. Secondly, the thorny porous tubular structure can provide reactant substances of different size transport circumstances comparable to those in open medium and expedite mass transportation, so the chemical reactions can happen more easily.[45–47] Thirdly, the thorny porous tubular structure can allow multiple reflections of simulated solar light, which enhances light-harvesting and thus increases the quantity of photogenerated electrons and holes available to participate in the photocatalytic degradation of phenol.[48,49] In addition, Ag nanoparticles can act as electron traps to facilitate the separation of photogenerated electron-hole pairs and promote interfacial electron transfer process.[25,50] Moreover, one can see that the photocatalytic activity of the Ag–AgBr/TiO_2 samples increases gradually with the increase of the AgBr precursor content, the 10%Ag–AgBr/TiO_2 catalyst showed the highest photocatalytic activity. With further increasing the AgBr precursor content, the photocatalytic activity of the Ag–AgBr/TiO_2 samples gradually decreased again. In comparison with the 10%Ag–AgBr/TiO_2, the 5%Ag–AgBr/TiO_2 displays a high charge separation rate, and the 15%Ag–AgBr/TiO_2 and 20%Ag–AgBr/TiO_2 show high visible light absorption based on the results of the above SPS and UV-vis absorption spectra measurements, which demonstrates that the high photocatalytic activity depends on the combination effects of high charge separation rate and high light absorption. The results indicate that there is an optimal loading amount of AgBr precursor content.

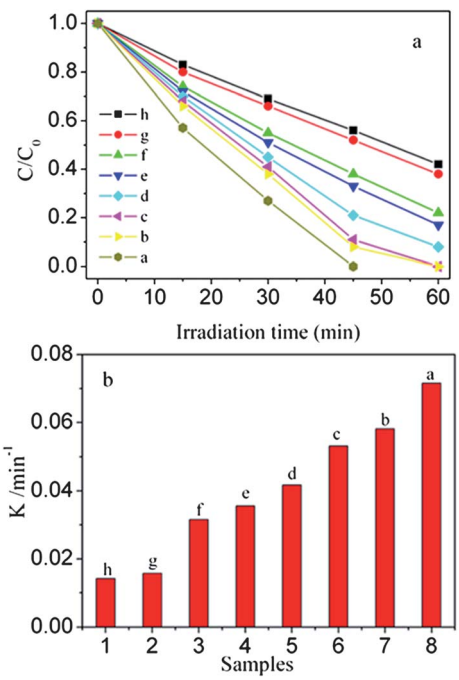

Fig. 9 Photocatalytic degradation of phenol as a function of irradiation time in the presence of different photocatalysts under simulated solar light irradiation (a) and the corresponding comparison of rate constant k (b). (a) 10%Ag–AgBr/TiO_2, (b) 5%Ag–AgBr/TiO_2, (c) crushed 10%Ag–AgBr/TiO_2, (d) 15%Ag–AgBr/TiO_2, (e) 20%Ag–AgBr/TiO_2, (f) 10%Ag–AgBr/Degussa P25, (g) thorny TiO_2 tubes, (h) Degussa P25.

In the Ag–AgBr/TiO_2 composite system, both TiO_2 and AgBr can be excited by the simulated solar light and have different photoabsorption ranges, so can enhance the utilization of the simulated solar light. A schematic diagram of the band levels of the Ag–AgBr/TiO_2 composite and the possible reaction mechanism of the photocatalytic procedure is given in Fig. S10.† Under simulated solar light irradiation, the electrons in the valence band (VB) of TiO_2 and AgBr are excited to the corresponding conduction band (CB). Then the electrons in the CB of TiO_2 migrate into the metal Ag (electron transfer I: TiO_2 to Ag) through the Schottky barrier because the CB of TiO_2 is higher than that of the loaded metal Ag, This process of electron transfer is faster than the electron-hole recombination between the VB and CB of TiO_2. Thus, the electrons in the CB of TiO_2 can be stored in the Ag component. Meanwhile, because the energy level of Ag is above the VB of AgBr, the holes in the VB of AgBr can also easily flow into metal Ag (electron transfer II: Ag to AgBr), which is faster than the electron-hole recombination between the VB and CB of AgBr. Therefore, simultaneous electron transfer I and II should occur as a result of simulated solar light excitation of both TiO_2 and AgBr, which is similar to previous reports.[40,51,52] As a result, the holes in the VB of TiO_2 with a strong oxidation power can particulate in photocatalytic reactions to directly degrade the organic pollutants, and the electrons in the CB of AgBr with a strong reduction power can be transferred to the adsorbed O_2 acting as an electron acceptor to form first the superoxide radical anions, $O_2^{\cdot-}$, finally forming HO· radicals.[44] These active species will result in the degradation of phenol.

Furthermore, the photocatalytic activities of the different Ag–AgBr/TiO_2 samples under visible light irradiation were also evaluated. As shown in Fig. S11,† when the UV light is filtered off from the simulated solar light irradiation source, the pure thorny TiO_2 tube sample shows no obvious photocatalytic activity. The decrease of phenol concentration is mainly due to photolysis. The sequences of photocatalytic activity were different from that under simulated solar light irradiation. Under visible light irradiation, the electrons from the plasmon-excited Ag nanoparticles transferred to the CB of AgBr and enhance the interfacial charge transfer. The $O_2^{\cdot-}$ radicals were generated by O_2 trapping the electron in the CB of AgBr coming from both the photoexcited AgBr and plasmon-photoexcited Ag nanoparticles. Therefore, the efficient degradation of phenol came from both the photoexcited AgBr and plasmon-excited Ag nanoparticles.

The photocatalytic activities of the Ag–AgBr/TiO_2 composite samples were enhanced with the increase of AgBr content. As the AgBr amount increased to 15%, the highest photocatalytic activity was achieved. However, the photocatalytic activity decreased when the AgBr content further increased, and this probably resulted from excessive trapping sites caused by the increased AgBr and Ag content in the Ag–AgBr/TiO_2 composite which facilitated the recombination of photoinduced electrons and holes.

The repeated photocatalytic experiments on the thorny 10% Ag–AgBr/TiO_2 composite were also examined. After six consecutive cycles of degradation experiments under simulated solar light irradiation, the photocatalytic activity only showed a slight decrease because the amount of the thorny 10%Ag–AgBr/TiO_2 composite in the reactor was slightly reduced due to the sampling of the slurry at every measurement of the phenol concentration (Fig. S12†). Comparison of the XANES (line c and f in Fig. S6†) and Fourier-transformed spectra of the k^2 weighted Ag K-edge EXAFS oscillations (line c and f in Fig. S7†) for the thorny 10%Ag–AgBr/TiO_2 composite before and after photocatalytic reaction show that there is no obvious change. The AgBr in the composite is not apparently destroyed during the photocatalytic process. The XPS spectrum (Fig. S13†) of Ag 3d of the thorny 10%Ag–AgBr/TiO_2 sample after six consecutive cycles of degradation experiments is almost identical to that of the as-prepared sample, and the calculated content (2.08 mol%) of the surface Ag^0 exhibits no obvious change in comparison with the sample before the photocatalytic experiments. These results indicate that the thorny 10%Ag–AgBr/TiO_2 composite system is an effective and stable catalyst under our experimental conditions. It is mainly ascribed to the fact that the presence of metal Ag can effectively inhibit the decomposition of AgBr under simulated solar light irradiation.

4. Conclusions

In summary, thorny Ag–AgBr/TiO_2 tube composites with high simulated solar-light activity were fabricated *via* the synthesis of thorny TiO_2 tubes using rod-like $TiOSO_4 \cdot 2H_2O$ as both the Ti source and sacrificial template, followed by deposition of AgBr nanoparticles on the TiO_2 surface and calcination. The prepared composites showed greatly enhanced simulated solar light photocatalytic activity, which is attributed to the migration efficiency of the photoinduced carriers at the interface of the composite and the enhanced efficiency of photo harvesting due to its special thorny tubular structure. XAFS, XANES, XPS and photocatalytic experimental results confirmed that the Ag–AgBr/TiO_2 composites were effective and stable photocatalysts under simulated solar light irradiation.

Acknowledgements

We gratefully acknowledge the support of the Key Program Projects of the National Natural Science Foundation of China (No. 21031001), the National Natural Science Foundation of China (No. 20971040, 91122018, 51102082, 21101060, 21001112), the Cultivation Fund of the Key Scientific and Technical Innovation Project, the Knowledge Innovation Program of Chinese Academy of Sciences, Ministry of Education of China (No. 708029), China Postdoctoral Science Foundation (20110490154), the Scientific Research Fund of Heilongjiang Provincial Education Department (No. 11541283, 12511376), The authors thank beamline BL14W1 (Shanghai Synchrotron Radiation Facility) for providing the beam time.

References

1 A. Fujishima and K. Honda, *Nature*, 1972, **238**, 37.
2 Z. F. Bian, J. Zhu, F. L. Cao, Y. F. Lu and H. X. Li, *Chem. Commun.*, 2009, 3789.
3 N. K. Allam, K. Shankar and C. A. Grimes, *J. Mater. Chem.*, 2008, **18**, 2341.
4 X. F. Li, T. X. Fan, H. Zhou, S.-K. Chow, W. Zhang, D. Zhang, Q. X. Guo and H. Ogawa, *Adv. Funct. Mater.*, 2009, **19**, 45.
5 M. Es-Souni, M. Es-Souni, S. Habouti, N. Pfeiffer, A. Lahmar, M. Dietze and C.-H. Solterbeck, *Adv. Funct. Mater.*, 2010, **20**, 377.
6 D. Eder, I. A. Kinloch and A. H. Windle, *Chem. Commun.*, 2006, 1448.
7 D. Chen, F. Huang, Y. B. Cheng and R. A. Caruso, *Adv. Mater.*, 2009, **21**, 2206.
8 Z. Y. Liu, X. T. Zhang, S. Nisimoto, T. Murakami and A. Fujishima, *Environ. Sci. Technol.*, 2008, **42**, 8547.
9 J. M. Macak, H. Tsuchiya and P. Schmuki, *Angew. Chem., Int. Ed.*, 2005, **44**, 2100.
10 H. Imai, Y. Takei, K. Shimizu, M. Matsuda and H. Hirashima, *J. Mater. Chem.*, 1999, **9**, 2971.
11 S. Kobayashi, N. Hamasaki, M. Suzuki, M. Kimura, H. Shirai and K. Hanabusa, *J. Am. Chem. Soc.*, 2002, **124**, 6550.
12 T. R. B. Foong, Y. D. Shen, X. Hu and A. Sellinger, *Adv. Funct. Mater.*, 2010, **20**, 1390.
13 G. P. Dai, J. G. Yu and G. Liu, *J. Phys. Chem. C*, 2011, **115**, 7339.
14 J. G. Yu, Q. L. Li, J. J. Fan and B. Cheng, *Chem. Commun.*, 2011, **47**, 9161.
15 G. L. Li, J. Y. Liu and G. B. Jiang, *Chem. Commun.*, 2011, **47**, 7443.
16 A. L. Linsebigler, G. Q. Lu and J. T. Yates, *Chem. Rev.*, 1995, **95**, 735.
17 T. Ohno, T. Mitsui and M. Matsumura, *Chem. Lett.*, 2003, **32**, 364.
18 X. Chen and C. Burda, *J. Am. Chem. Soc.*, 2008, **130**, 5018.
19 H. G. Yu, I. Hiroshi, S. Yoshiki, H. Yasuhiro, K. Yasushi, M. Miyauchi and H. Kazuhito, *J. Phys. Chem. C*, 2010, **114**, 16481.
20 H. Li, Z. Bian, J. Zhu, Y. Huo, H. Li and Y. Lu, *J. Am. Chem. Soc.*, 2007, **129**, 4538.
21 S. Vaidyanathan, E. W. Eduardo and V. K. Prashant, *J. Am. Chem. Soc.*, 2004, **126**, 4943.
22 Y. Hou, X. Y. Li, Q. D. zhao, X. Quan and G. H. Chen, *Environ. Sci. Technol.*, 2010, **44**, 5098.
23 M. D. Vasileia, A. Maria, L. Gianluca, I. K. Dimitris and L. Panagiotis, *Environ. Sci. Technol.*, 2010, **44**, 7200.
24 C. Hu, T. W. Peng, X. X. Hu, Y. L. Nie, X. F. Zhou, J. Qu and H. He, *J. Am. Chem. Soc.*, 2010, **132**, 857.
25 C. Hu, Y. Lan, J. Qu, X. Hu and A. Wang, *J. Phys. Chem. B*, 2006, **110**, 4066.
26 R. E. Mohammad, R. Sara, H. Saeed and R. G. Mohammad, *J. Am. Chem. Soc.*, 2007, **129**, 9552.
27 A. Koichi, F. Makoto, R. Carsten, T. Junji, M. Hirotaka, O. Yoshimichi, Y. Naoya and W. Toshiya, *J. Am. Chem. Soc.*, 2008, **130**, 1676.
28 M. Z. Xie, L. Q. Jing, J. Zhou, J. S. Lin and H. G. Fu, *J. Hazard. Mater.*, 2010, **176**, 139.
29 L. Q. Jing, B. F. Xin, F. L. Yuan, L. P. Xue, B. Q. Wang and H. G. Fu, *J. Phys. Chem. B*, 2006, **110**, 17860.
30 B. Ravel and M. Newville, *J. Synchrotron Radiat.*, 2005, **12**, 537.
31 C. Q. Wang, D. R. Chen and X. J. Jiao, *J. Phys. Chem. C*, 2009, **113**, 7714.
32 D. Larcher, R. Sudant, R. Patrice and J.-M. Tarascon, *Chem. Mater.*, 2003, **15**, 3543.
33 G. H. Tian, Y. J. Chen, W. Zhou, K. Pan, C. G. Tian, X.-R. Huang and H. G. Fu, *CrystEngComm*, 2011, **13**, 2994.
34 X. C. Jiang, Y. L. Wang, T. Herricks and Y. N. Xia, *J. Mater. Chem.*, 2004, **14**, 695.
35 J. A. Nucci, R. D. Field, P. Keller and Y. Shacham-Diamand, *Appl. Phys. Lett.*, 1997, **70**, 1242.
36 J. Lu, Y. Xie, F. Xu and L. Y. Zhu, *J. Mater. Chem.*, 2002, **12**, 2755.

37 P. Wang, B. B. Huang, X. Y. Qin, X. Y. Zhang, Y. Dai and M.-H. Whangbo, *Inorg. Chem.*, 2007, **46**, 6980.
38 Md. S. A. S. Shah, M. Nag, T. Kalagara, S. Singh and S. V. Manorama, *Chem. Mater.*, 2008, **20**, 2455.
39 F. L. Zhang, Y. H. Zheng, Y. N. Cao, C. Q. Chen, Y. Y. Zhan, X. Y. Lin, Q. Zheng, K. M. Wei and J. F. Zhu, *J. Mater. Chem.*, 2009, **19**, 2771.
40 L. S. Zhang, K.-H. Wong, Z. G. Chen, J. C. Yu, J. C. Zhao, C. Hu, C.-Y. Chan and P.-K. Wong, *Appl. Catal., A*, 2009, **363**, 221.
41 L. Q. Jing, Z. L. Xu, J. Shang, X. J. Sun, W. M. Cai and H. G. Fu, *Sol. Energy Mater. Sol. Cells*, 2003, **79**, 133.
42 Y. H. Lin, D. J. Wang, Q. D. Zhao, M. Yang and Q. L. Zhang, *J. Phys. Chem. B*, 2004, **108**, 3202.
43 L. Q. Jing, H. G. Fu, B. Q. Wang, D. J. Wang, B. F. Xin, S. D. Li and J. Z. Sun, *Appl. Catal., B*, 2006, **62**, 282.
44 L. Kronik and Y. Shapira, *Surf. Sci. Rep.*, 1999, **37**, 1.
45 J. G. Yu, G. P. Dai and B. B. Huang, *J. Phys. Chem. C*, 2009, **113**, 16394.
46 D. R. Rolison, *Science*, 2003, **299**, 1698.
47 S. Y. Zeng, K. B. Tang, T. W. Li and Z. H. Liang, *J. Phys. Chem. C*, 2010, **114**, 274.
48 L. Zhang and J. C. Yu, *Chem. Commun.*, 2003, 2078.
49 H. X. Li, Z. F. Bian, J. Zhu, D. Q. Zhang, G. S. Li, Y. N. Huo, H. Li and Y. F. Lu, *J. Am. Chem. Soc.*, 2007, **129**, 8406.
50 J. Ren, W. Z. Wang, S. M. Sun, L. Zhang and J. Chang, *Appl. Catal., B*, 2009, **92**, 50.
51 H. Tadai, T. Mitsui, T. Kiyonagai, T. Akita and K. Tanaka, *Nat. Mater.*, 2006, **5**, 782.
52 V. Subramanian, E. E. Wolf and P. V. Kamat, *J. Am. Chem. Soc.*, 2004, **126**, 4943.

